Supporting Information

Puchner *et al.* 10.1073/pnas.0805034105

SI Text

1. Expression and Purification of Titin Kinase. Three titin kinase constructs were expressed for this study: A168-M2 (867 aa, from 24422 to 25288 in human cardiac N2-B titin, accession number NP_003310.3); A168-M2 K36A, where lysine 24783 is mutated to alanine; and TK-kin3 (314 aa, from 24725 to 25038 in NP_003310.3), where the autoregulatory tail is partially removed to expose the ATP binding site (2). The boundaries of TK-kin3 mimic the mechanically opened state where the autoinhibitory tail is removed apart from the mechanostable αR1 helix (see molecular dynamics section for details). The numbering of the constructs can be converted to that of the amino acids in the titin kinase structure [Protein Data Bank (PDB) entry 1TKI] by subtracting 24747 from the amino acid numbers in N2B titin NP_003310.3, respectively, by adding 24747 to the numbers in 1TKI. A conversion table for residues discussed in the manuscript is given in Table S1. The cDNAs encoding these constructs were cloned into a modified baculovirus shuttle plasmid and N-terminally fused to a tag sequence encoding, from the N terminus, a hexa-histidine tag, HA-tag, and TEV cleavage site. Constructs were verified by DNA sequencing. After generation of recombinant virus, expression was carried out in suspension cultures of *Spodoptera frugiperda* sf9 cells essentially as described (3). Soluble protein was purified at a yield of 6 mg/liter of culture for A168-M2, and 20 μg/liter for TK-kin3 and purified by sequential nickel-affinity chromatography, ion-exchange chromatography on a Mono Q column, and size-exclusion chromatography on a Superdex 75 column (GE Healthcare). For some experiments, the His-tag sequence was cleaved off by TEV protease, but the presence or absence of the tag had no detectable influence on kinetic parameters or unfolding characteristics. Final fractions were >99.5% pure as judged from overloaded gels (Fig. S1). Protein was stored in small aliquots at a concentration of 1 mg/ml in 20 mM 2-[4-(2-hydroxyethyl)-1-piperazine]ethanesulfonic acid (Hepes)/KOH (pH 7), 2 mM $MgCl_2$, 50 mM NaCl, 2 mM DTT, and 10% glycerol in liquid nitrogen. Identity of the proteins was ascertained by gel electrophoresis, analytical gel filtration, Western blots using anti-titin kinase antibodies (4), and mass spectrometry (MS). MS confirmed not only the correct molecular weight for TK-kin3, but also detected two bound magnesium ions in this open form of the kinase, indicating that protein kinases bind Mg^{2+} independently of ATP. Kinase assays with recombinant telethonin showed that only kin3, but not the long forms of the kinase, showed protein kinase activity *in vitro*.

2. Kinase Assays. Michaelis–Menten kinetics of TK was performed similarly as described for phosphorylase kinase (5) but using telethonin as substrate at a constant concentration of 10 μM in assay buffer [20 mM Hepes/KOH (pH 7), 5 mM $MgCl_2$, 5 mM DTT]. ATP concentrations varied from 165 nM to 800 μM for kinetic analysis with a constant 165 nM [γ-^{33}P]ATP label. Samples were taken from triplicate assays at regular intervals from 20-μl reaction mixtures, spotted on nitrocellulose, and immediately quenched in 5% ice-cold trichloroacetic acid (TCA). After several washes with TCA, the filters were dried and protein-incorporated radioactivity determined by liquid scintillation counting. After correction for background (label and telethonin, no enzyme), the averaged protein phosphorylation rate expressed as μmol/minute was fitted to the Michaelis–Menten equation by using Mathematica, and K_M was derived. Results are summarized in Table 1.

3. Autophosphorylation of Titin Kinase. Highly purified TK kin3 (see above) was incubated at 30°C in assay buffer supplemented with 0.1 mM sodium orthovanadate in the absence and presence of ATP, with either 5 mM Mg^{2+} or Mn^{2+} as counterion (6). The reaction was stopped after 20 min by addition of Laemmli sample buffer, and the samples were electrophoresed on 14% SDS-polyacrylamide gels. After Western blotting of the gels by standard procedures, phosphotyrosine was detected by using the 4G10 monoclonal antibody (Upstate Biotechnology) and a site-specific anti-titin kinase antibody raised against the peptide APEYY(PO_4)APE, which specifically reacts with titin kinase phosphorylated on tyrosine 170.

Both antibodies detect the formation of phosphotyrosine under these conditions, and autoradiographs of assays in the presence of [γ-^{33}P]ATP demonstrate label incorporation. Similar assays were performed at several enzyme concentrations (0.5, 1, 2, and 5 μM) in the presence of 165 nM [γ-^{33}P]ATP label and 100 μM total ATP, and TK-incorporated radiolabel was determined as above to test for concentration dependence of phosphate incorporation. The correlation of label incorporation was linear with enzyme concentration, suggesting that the phosphorylation occurred intramolecularly (7).

Atomic Force Microscopy (AFM) Measurements

4. AFM Sample Preparation. Microscope slides were washed with denatured ethanol and H_2O_{dd} in a supersonic bath. After drying, a layer of 4-nm Cr/Ni followed by a layer of 40-nm Au was evaporated onto the surface. Twenty microliters of the protein solution (1 mg/ml) was incubated for 20 min on the gold surface and washed three times with the measurement buffer, consisting of 40 mM Hepes/KOH, 2 mM $MgCl_2$, 2 mM DTT (pH 7.2), and, depending on the experiment, 2 mM ATP.

5. AFM Measurements. All force spectroscopy measurements were performed with a custom-built and completely automated AFM (Fig. S2). The instrument is controlled with an Asylum Research MFP3D controller and Igor Pro 5.0 (WaveMetrics). The software was written such that it automatically adjusts the height of the AFM and the position of the photodiode to compensate for instrument and cantilever drift. If an experiment is performed at several pulling speeds, the software periodically changes the speed after each force extension trace to allow a better comparison. In this way, force extension traces can be recorded for several days with the same sample and the same cantilever. To avoid evaporation of the buffer, a fluid cell consisting of Teflon and a latex membrane seals the probe volume during the experiment.

After calibration of the cantilevers (Olympus biolevers A) using the equipartition theorem (8), the automated measurement was started as described above. Because the surface is not homogeneously covered with the non-specifically adsorbed protein constructs, the *x*–*y* scanner of the AFM moves the sample by 20 nm after each trace. In this way, the number of traces showing unfolding of the protein construct is enhanced and in each trace a new molecule is picked up that was not unfolded before.

6. Selection of Traces. In single-molecule force spectroscopy experiments, the density of molecules attached to the surface has to be low enough to address individuals. Therefore, in ≈95% of measurement cycles, the approach of the cantilever to the surface does not result in a contact with a molecule. Furthermore, the protein construct is contacted at random positions

resulting in traces that do not show unfolding of the complete titin kinase. Because the protein construct contains three domains at the N terminus of the titin kinase and two on its C terminus, all traces showing more than three domains must contain the unfolding of the complete enzyme. Because of the small tip radius of the AFM cantilever (30 nm), traces showing more than one protein construct in parallel are very rare. They can be identified by the higher forces and by the superposition of their unfolding patterns that are in most of the cases shifted with respect to each other. In total, ≈1% of the recorded traces show the unfolding of one individual titin kinase molecule and are therefore selected for further analysis.

Because of the large amount of traces recorded for this study, and the low efficiency of complete unfolding traces due to the reasons mentioned above, we developed a method that allows automated selection of traces and recognition of unfolding patterns (1). In a first step, force extension traces are transformed into contour length space by using the QM-WLC model (9). In the next step, contour length histograms are obtained that directly reflect the barriers of the unfolding potential. This fingerprint is independent of fluctuations and variable experimental parameters and therefore can be used to screen for characteristic patterns. In this study, we adjusted the parameters such that only traces were selected showing more than three Ig-domains with a barrier spacing of ≈30 nm.

Because the folded protein construct is contacted at random positions, the initial part of a force extension varies in length. This variable offset can be determined choosing the rupture of the first Ig-domain as the point of reference. This has to be taken into account in superpositions of force extension traces or averaged barrier position histograms (Fig. S3). Once we identified the complete unfolding pattern of the titin kinase, we also took traces into account that show less than four Ig-domains but contain the complete unfolding pattern of the enzyme. In these cases, the protein construct was either picked up at its ends but de-adsorbed before all domains were unfolded, or it was contacted at the surrounding domains so that complete unfolding of the titin kinase took place.

Overview of the number of recorder traces. Recorded total traces, 392,000; total traces with some captured "bait," ≈30,000; total complete kinase traces, 2,100. Therefore, in ≈95% of measurement cycles, the approach of the cantilever to the surface does not result in a contact with a molecule. Because of the random attachment of the molecules, a substantial number of these traces are incomplete and contain mostly just some Ig/Fn domain unfolding signatures.

Traces with complete kinase signature used for analysis were as follows: kinetics with WT, 812 complete kinase traces; kinetics with K72A mutant, 962 complete kinase traces; concentration series with WT, 275 complete kinase traces; concentration series with K72A mutant, 348 complete kinase traces.

7. Molecular Calibration by Using Ig/Fn Domains. To confirm the proper calibration of the AFM, we compare the experimental contour length increments of Ig/Fn domain unfolding with the expected ones. The theoretical values are obtained in the following way. First, the number of folded amino acids is multiplied by 0.365 nm (corresponding to the separation of the Cα atoms of two adjacent amino acids in the completely extended conformation), which results in the complete contour length of the protein domain. In the next step, the diameter of the folded domain is subtracted from the complete contour length to obtain the experimentally visible contour length. This can be better seen if the gedanken experiment is performed backwards: if the two ends of a completely stretched Ig/Fn domain are brought together until the domain is in its globular folded conformation, then the distance between the attachment points corresponds with the diameter of the folded domain. Because this conformation is the starting point for the length measurement, the domain diameter is missing and has therefore to be subtracted from the complete contour length if compared with the experimental one (Table S2). The theoretical mean contour length of 30.86 nm deviates from the experimental one, determined in Fig. S4 to be 30.45 nm, by only 1%.

8. Influence of Ig Domains on the Unfolding Pattern. The use of spacer domains that provide their fingerprint for the selection of force extension traces has become a widespread approach (10). Although the unfolding pattern of these spacer domains is well studied, we verified the interpretation of force extension traces by performing experiments with TK protein constructs containing three and five spacer domains. As can be seen in Fig. S5, the maximum number of equal intervals corresponding to a contour length increment of ≈30 nm perfectly correlates with the number of spacer domains. Although the initial part of titin kinase unfolding is not so clearly resolved with *Escherichia coli*-expressed protein constructs (most likely because of folding differences, in agreement with *E. coli*-derived protein being catalytically inactive), this experiment justifies the interpretation that allows to separate unfolding of the titin kinase from unfolding of spacer domains.

9. Unfolding Behavior of the Titin Kinase at 37°C. Although also the titin of cold-blooded animals contains the titin kinase domain (e.g., frogs and fish), we investigated the unfolding pattern of the TK protein construct at 37°C. For these measurements, the whole AFM setup was put into a temperature-controlled oven, where force extension traces were recorded. We found that the unfolding forces of the titin kinase are smaller (≈30 pN) than at room temperature (≈50 pN) because the energy barriers are overcome more easily due to the higher thermal energy. This observation is consistent with other studies (11, 12). However, the unfolding pattern was found to be the same as the one observed at room temperature (Fig. S6). Therefore, we conclude that the structure and function of titin kinase is the same at both temperatures, allowing its investigation under the experimentally more stable conditions.

10. Detection of Force-Induced ATP Binding and Determination of the Reaction Kinetics. As shown, binding of ATP to the titin kinase causes an additional energy barrier in the unfolding pathway. By counting the traces showing this barrier, the relative frequency of ATP binding can be determined. Because the activation is mechanically triggered, the binding process takes place in chemical nonequilibrium and can be described as follows. Let TK* be the activated enzyme with accessible binding pocket and TK*:ATP the titin kinase–ATP complex. Then, the probability $P_{\mathrm{TK^*:ATP}}(t)$ of finding the complex after a reaction time t is given by the simple differential equation

$$\frac{dP_{\mathrm{TK^*:ATP}}(t)}{dt} = k_{\mathrm{on}}[\mathrm{ATP}] - k_{\mathrm{off}}P_{\mathrm{TK^*:ATP}}(t), \qquad [1]$$

where k_{on} and k_{off} are the association and the dissociation rates of ATP. Solving this equation yields

$$P_{\mathrm{TK^*:ATP}}(t) = \frac{k_{\mathrm{on}}}{k_{\mathrm{on}} + k_{\mathrm{off}}}\left(1 - e^{-(k_{\mathrm{on}}+k_{\mathrm{off}})t}\right). \qquad [2]$$

This model perfectly describes our experimental data and allows us to determine the kinetic parameters of ATP binding. The experimental time scale is given by the inverse ratio of the pulling speed and the extension increase, during which the ATP binding pocket is accessible and still correctly folded. This extension increase was determined with MD simulations and values 18 nm. The errors of the experimentally determined kinetic parameters

are mainly due to the fact that a limited number of random samples is available. Therefore, the errors are calculated by using the beta function and assuming a 95% confidence interval to be certain.

11. Molecular Dynamics (MD) Simulations. All simulations were carried out with the GROMACS simulation suite (13, 14), using the OPLS all-atom force field (15) and periodic boundary conditions. NpT ensembles were simulated, with the protein and solvent coupled separately to a 300-K heat bath (τ_T = 0.1 ps) (16). The systems were isotropically coupled to a pressure bath at 1 bar (τ_p = 1.0 ps) (16). Application of the Lincs (17) and Settle (18) algorithms allowed for an integration time step of 2 fs. Short-range electrostatic and Lennard–Jones interactions were calculated within a cut-off of 1.0 nm, and the neighbor list was updated every 10 steps. The particle mesh Ewald (PME) method was used for the long-range electrostatic interactions (19), with a grid spacing of ≈0.12 nm.

12. ATP Force Field. The atomic partial charges of ATP used along with the OPLS force field were derived from quantum chemical calculations. The charges were obtained from B3LYP/6–31+G* calculations using the CHELPG electrostatic potential fitting scheme (20). The quantum chemical calculations were carried out with Gaussian 03 (21). All nonbonded parameters are given in Tables S3 and S4. Bonded parameters were taken from ref. 22.

13. Generation of Starting Structure. The simulations of the full-length titin kinase (TK) were set up as described in ref. 23, with the exception that, here, the OPLS force field was used (see above).

The starting structures of the truncated TK were obtained from the TK crystal structure (PDB entry 1TKI) (3) in three steps detailed below. First, 33 residues at the C terminus comprising the βR1 and αR2 motives of the autoinhibitory tail (ai tail) were removed from the structure, because they block the ATP binding site. Second, the ATP ligand was docked into the active site. Third, the ligand-induced conformational closure of the protein structure was enforced by MD.

14. Docking of ATP. ATP was docked into the active site of TK by using the protein kinase A (PKA) (PDB entry 1Q24) (24) as a homology model. After aligning of the two protein structures, the ATP and one Mg^{2+} ion were adopted from PKA. The second Mg^{2+} ion was added by using the phosphorylase kinase structure as a template (PDB entry 2PHK) (25), because it was not resolved in the PKA structure.

15. Energy Minimization and Equilibration of the Solvent. Before the free MD simulations, the systems were solvated with TIP4P water within a cubic box of 8.5 nm length. Sodium and chloride ions were added ($c \approx 0.15$ mol/liter), and the systems were energy-minimized for 1,000 steps by using steepest descent. The solvent was then equilibrated for 500 ps with positional restraints on the protein heavy atoms (force constant 1,000 kJ·mol^{-1}·nm^{-2}).

16. Closure of the Active Site. The ligand-induced conformational closure of the protein structure was enforced by means of essential-dynamics MD (26). To this end, the closed conformation of the PKA (1Q24) was used as the target structure. First, the two protein structures (TK and PKA) were aligned. Then, the N-terminal β-hairpin (residues 13–21 in TK) was selected, and a principal component analysis (PCA) was carried out, yielding one eigenvector that describes the closing motion. Essential dynamics sampling was then performed, during which motion along the eigenvector toward the target structure was enforced [radcon option in EDsampling module (27) of GROMACS]. To allow the protein to relax along the enforced closing motion, the maximal step size along the eigenvector was restricted to a maximum of 0.05 pm per step, leading to a closed structure within ≈1 ns. Subsequently, the closed structure was simulated for 1 ns with positional restraints on the C^{α} atoms (force constant 1,000 kJ·mol^{-1}·nm^{-2}). Finally, a 1-ns free MD simulation was carried out, during which no opening motion was observed in the presence of ATP. As a control, the closed structure was simulated also in the absence of ATP. As expected, significant reopening motion was observed. The starting conformation for the force-probe MD simulations were taken from the final free MD simulations after 1 ns.

In the resulting structure with ATP bound, a salt bridge between Lys-36 and the α-phosphate group of ATP, and interaction between Met-34 and the adenine moiety, respectively, were formed. For the latter, two types of interactions with ATP are seen, a hydrogen bond between the sulfur atom and the NH_2 group of adenine, and, alternatively, a stacked conformation of the S-CH_3 group and the adenine 6-ring. Additional hydrogen bonds were formed between the β-phosphate of ATP and the N-H backbone of Glu-17, as well as between the hydroxyl groups of the ribose and the carbonyl backbone of Arg-15.

17. Force–Probe MD Simulations. To mimic the AFM experiments, force–probe MD simulations (FPMD) were carried out (28, 29). In these simulations, a harmonic spring was attached to the carbon atom of the carboxyl C terminus and one to the nitrogen atom of the amino N terminus, each described by a spring potential,

$$V_{\text{spring},i}(t) = \frac{k_0}{2}\,(z_i - z_{\text{spring},i}(t))^2, \qquad [3]$$

which was included within the force field. In Eq. **3**, k_0 = 500 kJ·mol^{-1}·nm^2 is the force constant of the spring, z_i is the position of the pulled atom i, and $z_{\text{spring},i}$ is the position of the spring that is attached to atom i. The springs were then moved with constant velocity v = 0.4 m/s in opposite directions, $z_{\text{spring},i}(t) = z_i(0) \pm vt$. Because of the moving springs, the pulled atoms experienced an additional force

$$F_i = k_0(z_i - z_{\text{spring},i}(t)). \qquad [4]$$

The average force at the two springs was monitored during the simulations, yielding the force profiles shown in Fig. 3*B*.

Before the FPMD simulations, the protein was aligned along the pulling direction (z axis), and the simulation box was extended along the z axis to ≈20 nm, allowing for the accommodation of an elongated conformation. Further, water, sodium, and chloride ions ($c \approx 0.15$ mol/liter) were added, and the system was energy-minimized, followed by equilibration for 200 ps with positional restraints on the protein heavy atoms (force constant 1,000 kJ·mol^{-1}·nm^{-2}).

To generate statistically independent unfolding trajectories (five trajectories with and without ATP, respectively), a partially unfolded conformation was selected after 19.2 and 20.2 ns of FPMD simulation time with and without ATP, respectively. These conformations were chosen because they correspond to minima in the force profiles. The nitrogen atom of the N terminus and the carbon atom of the C terminus, respectively, were kept fixed with a positional restraint (force constant 1,000 kJ·mol^{-1}·nm^{-2}), and the systems were equilibrated for 1 ns with free MD. From this trajectory, five equidistant frames (Δt = 200 ps) were chosen as starting structures for the additional force–probe simulations.

Simulations were interrupted before any of the springs had crossed the box boundary. Here, care was taken that, because of the applied periodic boundary conditions, the pulled termini did

not interact with each other. At this point, fully unfolded residues at both termini were removed, and new termini, water, and ions were added. The FPMD simulations were then continued after equilibration of the solvent with positional restraints on the protein heavy atoms (force constant 1,000 kJ·mol^{-1}·nm^{-2}) for 200 ps.

The simulated systems comprised ≈180,000 atoms. The total simulation time was ≈500 ns.

18. Contour Length Plots. The plotted contour lengths aim at quantitative comparison between the simulations and the experiments. Such comparison is complicated by the fact that (*i*) different pulling speeds are used and, (*ii*) in the simulations, a stiffer spring has to be used then in the AFM experiments. To account for these differences, we derived contour length plots from the force profiles obtained from the MD simulations in three steps. First, prominent force peaks were selected along the force profiles. Here, only those force peaks j were included whose height $F_{\max,j}$ exceeded a certain threshold. This threshold was defined as

$$F_{\max,j} \geq F_{\max,j-1} - k_{\mathrm{AFM}}\,(\Delta z_{\mathrm{spring},j} - \Delta z_{\mathrm{spring},j-1}\,(t)), \qquad [5]$$

where k_{AFM} is the effective spring constant of the AFM cantilever and the attached linkers, and $\Delta z_{\mathrm{spring}}$ is the distance between the two springs attached to the C and N terminus, respectively, and $j - 1$ denotes the force peak preceding peak j. Here, k_{AFM} was estimated as 10 pN/nm, which is an upper limit. This selection procedure mimics the effect of the soft AFM cantilever, which, in contrast to the force probe simulations, is insensitive to minor force peaks that immediately follow a larger peak. Second, the number of unfolded residues $N_{\mathrm{unf},j}$ and the length of the folded core $\Delta z_{\mathrm{folded},j}$ were determined for the conformations corresponding to each of these peaks. The contour length $l_{c,j}$ was then calculated as $l_{c,j} = N_{\mathrm{unf},j} \times 0.365$ nm + $\Delta z_{\mathrm{folded}}$. Third, a Gaussian function was assigned to each of the peaks, weighted by its height $F_{\max,j}$:

$$G_j(l_c) = F_{\max,j} \exp\left(\frac{(l_c - l_{cj})^2}{2\sigma^2}\right), \qquad [6]$$

with a width $\sigma = 1$ nm. The final contour length plot is obtained from the sum of all these Gaussian functions. As an exception, this procedure was not applied to the force peak marked with a plus sign in Fig. 3*B Top*. Structural analysis shows that peak arises from transient rupture and reformation of the interactions between Lys-36/Met-34 and ATP, similar to the subsequent ATP peak 2*. From the considerable scatter of heights seen for peak 2*, we expect that the peak in question is exceptionally pronounced and, therefore, that the described shadowing effect will not occur in most of the cases. No other peak showed a similar effect.

Fig. 4 compares the contour lengths from experiment and MD simulation. For direct comparison, one has to consider that the AFM measurements were conducted with a full TK that additionally includes a linker of 23 residues. No structural information was available for this 23-residue linker between A170 and the catalytic core. In the homologous twitchin kinase, this sequence wraps around the ATP binding lobe of the kinase but makes no contacts with the autoregulatory domain. We therefore expect this part to affect the relative positions of the observed unfolding peaks but not the sequence of local unfolding events at the C terminus. In fact, the contour length difference of 9 nm between peaks 1 and 2 corresponds the 23-residue linker length, which provided further support for our assignment. In the MD simulations, either a full-length TK or a truncated TK—i.e., with a part of the autoinhibitory tail removed—was used. As a reference point for comparison, peak 6 was chosen, which indicates unfolding of Ig-domain "handles" at a fully unfolded TK (l_c = 144.4 nm). The 321 residues of the full TK or the 289 residues of the truncated TK would all be unfolded at this point. The simulations allow assigning the ATP peak (peak 2*) to the anchor point Lys-36. Thus, 289 − 36 = 253 residues unfold between peaks 2* and 6, which corresponds to a contour length increment of 253 × 0.365 nm = 92 nm. Including the length of the folded core of 5.5 nm, this estimate yields an l_c for peak 2* of 144.4 nm − 92 nm + 5.5 nm = 57.9 nm from the simulations, in good agreement with the value of 51.6 nm from the AFM.

The above procedure rests on two assumptions. First, we assume that before peak 2*, all N-terminal residues before Lys-36 unfold. In addition, by simulating a truncated TK, we assume that unfolding of the omitted part of the autoinhibitory tail is uncoupled from the other unfolding events and precedes peak 2*. Both assumptions are corroborated by the simulations of the complete TK, where such an unfolding behavior was indeed observed (see Fig. 3).

The simulations of the complete TK also show that peak 2 can be assigned to the unfolding of the autoinhibitory tail (Fig. 3). Hence, the first part of the contour length profile shown in Fig. 4 *Inset* is based on these simulations. Here, Tyr-7 was chosen as an anchor point, a residue that lies at the beginning of βR1. Following the same argumentation as outlined above, this choice yields a barrier position for peak 2 of 35.5 nm, in good agreement with the 32.3 nm obtained from the AFM data. We note that, in contrast to peak 2*, where the anchor point can be easily assigned to the Met-34/Lys-36 motive, such a detailed assignment is more challenging for peak 2. Here, only a range of βR1 residues between Glu-5 and Asp-12 can be specified, thus leading to an uncertainty in the position of peak 2 of ≈1.5 nm.

Fig. S7 compares the barrier positions obtained from the AFM experiments and the two independent MD simulations of the complete TK in the absence of ATP (Fig. 3*B Bottom*). The MD simulations yield positions of peaks 2, 3, 4, and 5 at 35.5, 63.3, 80.1, and 86.8 nm, respectively. The corresponding peak positions obtained from the AFM experiments are 32.3, 61.3, 68.6, and 86.6 nm, respectively. For the force peaks 2, 3, and 5, the positions obtained from the simulations agree well with those obtained from the experiments, taking into account that the former are based on only two independent simulations. For peak 4, the difference between the simulations and the experiments is somewhat larger. We speculate that this difference results from the underlying free energy landscape that, at such partially unfolded conformations, is shallow and exhibits many barriers of comparable height along various unfolding directions, such that the pathways followed in the individual trajectories are different. Such heterogeneity of unfolding pathways is indeed seen from the color-coded unfolding events in Fig. 3*B Bottom*. A much larger number of trajectories would be required to thoroughly characterize this region of the energy landscape, which, however, is not the focus of this work.

1. Puchner EM, Franzen G, Gautel M, Gaub HE (2008) Comparing proteins by their unfolding pattern. *Biophys J* 95:426–434.
2. Lange S, *et al.* (2005) The kinase domain of titin controls muscle gene expression and protein turnover. *Science* 308:1599–1603.
3. Mayans O, *et al.* (1998) Structural basis of the activation of the titin kinase domain during myofibrillogenesis. *Nature* 395:863–869.
4. Obermann WMJ, *et al.* (1996) The structure of the sarcomeric M band: Localization of defined domains of myomesin, M-protein and the 250 kD carboxy-terminal region of titin by immunoelectron microscopy. *J Cell Biol* 134:1441–1453.
5. Skamnaki VT, *et al.* (1999) Catalytic mechanism of phosphorylase kinase probed by mutational studies. *Biochemistry* 38:14718–14730.
6. Wedegaertner PB, Gill GN (1989) Activation of the purified protein tyrosine kinase domain of the epidermal growth factor receptor. *J Biol Chem* 264:11346–11353.

7. Tennagels N, Hube-Magg C, Wirth A, Noelle V, Klein HW (1999) Expression, purification, and characterization of the cytoplasmic domain of the human IGF-1 receptor using a baculovirus expression system. *Biochem Biophys Res Commun* 260:724–728.
8. Butt HJ, Jaschke M (1995) Calculation of thermal noise in atomic force microscopy. *Nanotechnology* 6:1–7.
9. Hugel T, Rief M, Seitz M, Gaub HE, Netz RR (2005) Highly stretched single polymers: Atomic-force-microscope experiments versus ab-initio theory. *Phys Rev Lett* 94:048301.
10. Dietz H, Rief M (2004) Exploring the energy landscape of GFP by single-molecule mechanical experiments. *Proc Natl Acad Sci USA* 101:16192–16197.
11. Janovjak H, Kessler M, Oesterhelt D, Gaub H, Muller DJ (2003) Unfolding pathways of native bacteriorhodopsin depend on temperature. *EMBO J* 22:5220–5229.
12. Schlierf M, Rief M (2005) Temperature softening of a protein in single-molecule experiments. *J Mol Biol* 354:497–503.
13. Van Der Spoel D, *et al.* (2005) GROMACS: Fast, flexible, and free. *J Comput Chem* 26:1701–1718.
14. Hess B, Kutzner C, van der Spoel D, Lindahl E (2008) GROMACS 4: Algorithms for highly efficient, load-balanced, and scalable molecular simulation. *J Chem Theory Comput* 4:435–447.
15. Jorgensen WL, Tirado-Rives J (1988) The OPLS potential functions for proteins. Energy minimizations for crystals of cyclic peptides and crambin. *J Am Chem Soc* 110:1657–1666.
16. Berendsen HJC, Postma JPM, van Gunsteren WF, DiNola A, Haak JR (1984) Molecular-dynamics with coupling to an external bath. *J Chem Phys* 81:3684–3690.
17. Hess B, Bekker H, Berendsen HJC, Fraaije GEM (1997) A linear constraint solver for molecular simulations. *J Comput Chem* 18:1463–1472.
18. Miyamoto S, Kollmann PA (1992) An analytical version of the SHAKE and RATTLE algorithms for rigid water models. *J Comput Chem* 13:952–962.
19. Darden T, York D, Pedersen L (1993) Particle mesh Ewald—An Nlog(N) method for Ewald sums in large systems. *J Chem Phys* 98:10089–10092.
20. Breneman CM, Wiberg KB (1990) Determining atom-centered monopoles from molecular electrostatic potentials—The need for high sampling density in formamide conformational-analysis. *J Comput Chem* 11:361–373.
21. Frisch MJ (2004) (Gaussian, Inc).
22. Klahn M, Schlitter J, Gerwert K (2005) Theoretical IR spectroscopy based on QM/MM calculations provides changes in charge distribution, bond lengths, and bond angles of the GTP ligand induced by the Ras-protein. *Biophys J* 88:3829–3844.
23. Grater F, Shen J, Jiang H, Gautel M, Grubmuller H (2005) Mechanically induced titin kinase activation studied by force-probe molecular dynamics simulations. *Biophys J* 88:790–804.
24. Gassel M, *et al.* (2003) Mutants of protein kinase A that mimic the ATP-binding site of protein kinase B (AKT). *J Mol Biol* 329:1021–1034.
25. Lowe ED, *et al.* (1997) The crystal structure of a phosphorylase kinase peptide substrate complex: Kinase substrate recognition. *EMBO J* 16:6646–6658.
26. Amadei A, Linssen AB, Berendsen HJ (1993) Essential dynamics of proteins. *Proteins* 17:412–425.
27. de Groot BL, Vriend G, Berendsen HJ (1999) Conformational changes in the chaperonin GroEL: New insights into the allosteric mechanism. *J Mol Biol* 286:1241–1249.
28. Grubmuller H, Heymann B, Tavan P (1996) Ligand binding: Molecular mechanics calculation of the streptavidin-biotin rupture force. *Science* 271:997–999.
29. Isralewitz B, Izrailev S, Schulten K (1997) Binding pathway of retinal to bacterio-opsin: A prediction by molecular dynamics simulations. *Biophys J* 73:2972–2979.

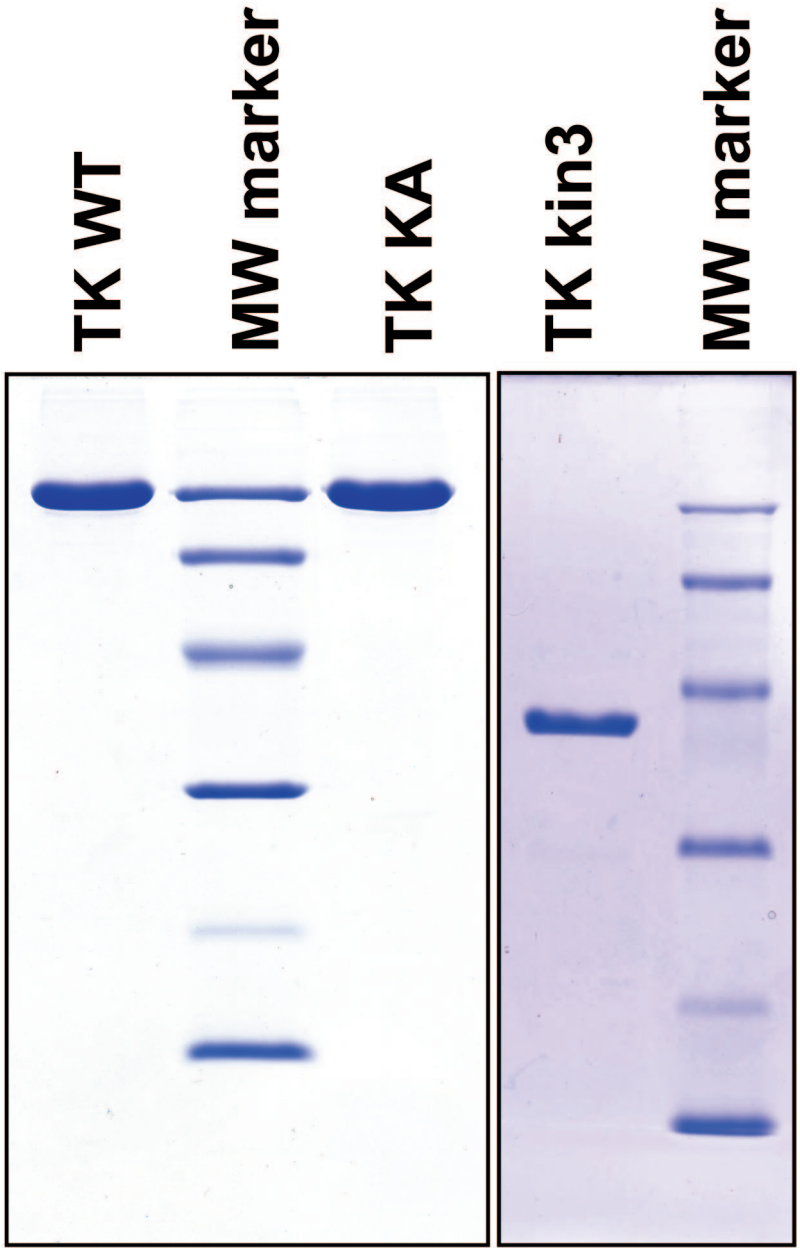

Fig. S1. (*Left*) Wild type (WT) and K36A mutant of the titin kinase A168-M2 construct after two-step purification; 2.5 μg of both WT and KA mutant titin kinase were loaded. (*Right*) Titin kinase domain kin3 after three-step purification; 1 μg was loaded. Molecular mass marker (in kDa), from top: 94, 64, 43, 30, 20, and 14.

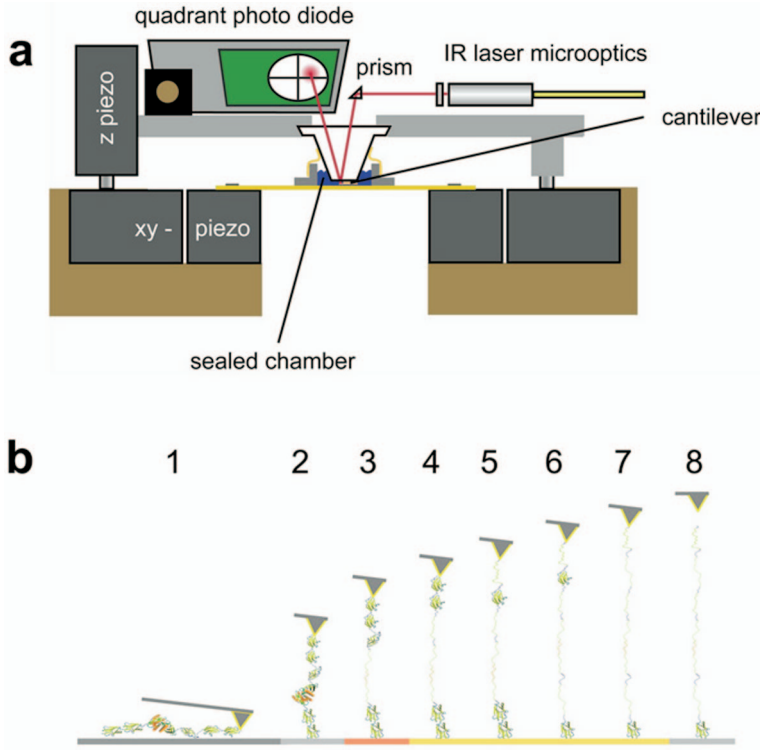

Fig. S2. (*a*) Schematics of the experimental setup. An IR laser is coupled through a fiber into the AFM head where it is focused onto the cantilever with a microoptic. The reflected beam is detected by a computer adjustable four-quadrant photodiode. The AFM head is moved up and down by a Z-piezo drive, and the sample is moved after each trace by a *x*–*y* piezo stage. To avoid evaporation of the buffer, we used a sealed measurement chamber. (*b*) Schematic overview of the AFM experiment showing the initial attachment of the protein to surface and cantilever (1), straightening of the protein to its folded length of ≈25 nm (2), unfolding of the kinase at low force (3), and sequential unfolding of the independently folding Ig and Fn3 domains at high forces (4–7). A rupture peak is observed when the completely unfolded peptide chain is pulled off the cantilever or surface (8).

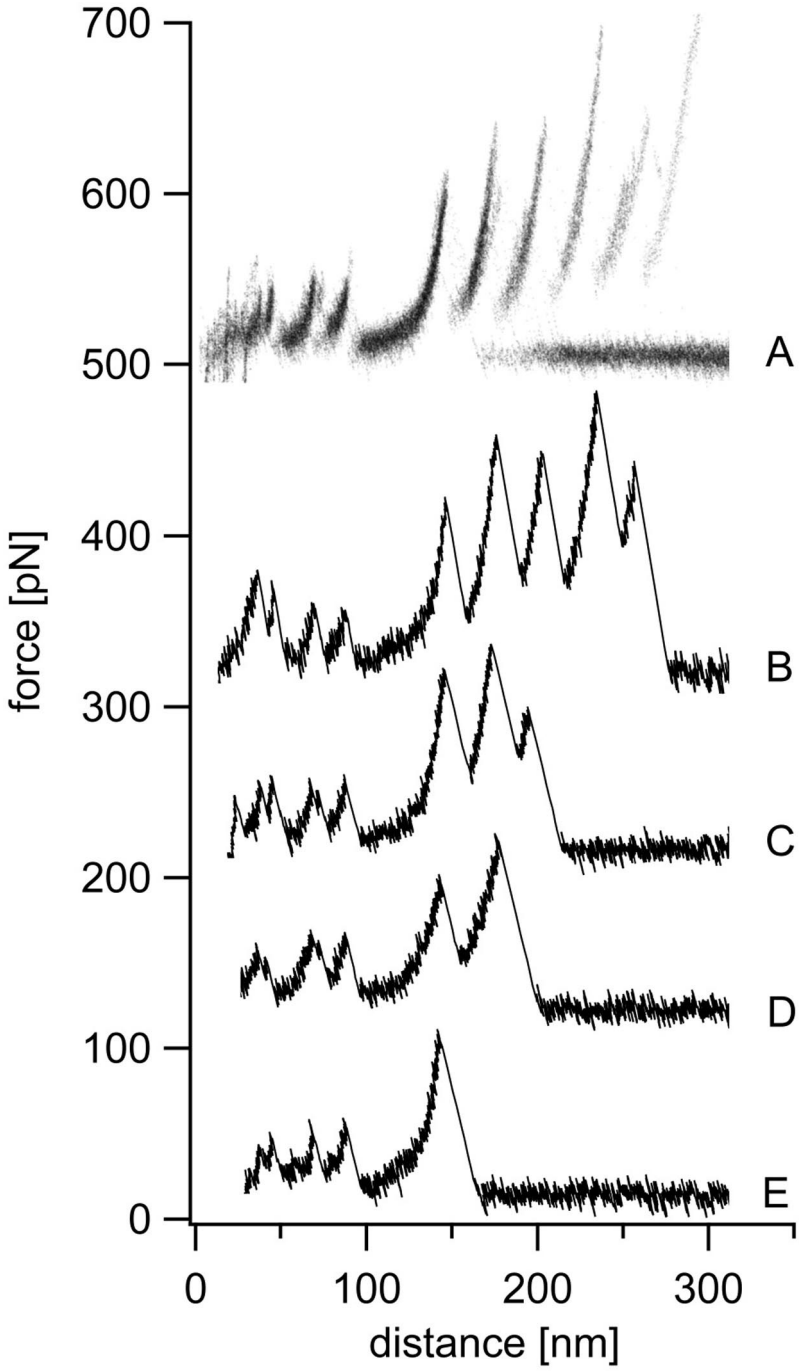

Fig. S3. Selection of traces and identification of the TK unfolding pattern in the absence of ATP. ''A'' is the superposition of traces showing the unfolding of one to five spacer domains and the complete unfolding pattern of the titin kinase domain. Traces are shifted with respect to each other whereas the rupture of the first Ig-domain served as the barrier of reference. In this way the different offsets in the initial part of the force extension traces, caused by rupture of spacer domain fragments and unspecific interactions, are taken into account. For clarity the points are plotted semitransparent. Once we identified the unfolding pathway of the titin kinase by means of traces showing more than three spacer domains (e.g., B), we took also traces into account exhibiting the complete unfolding pattern of the titin kinase but less spacer domains (C–E).

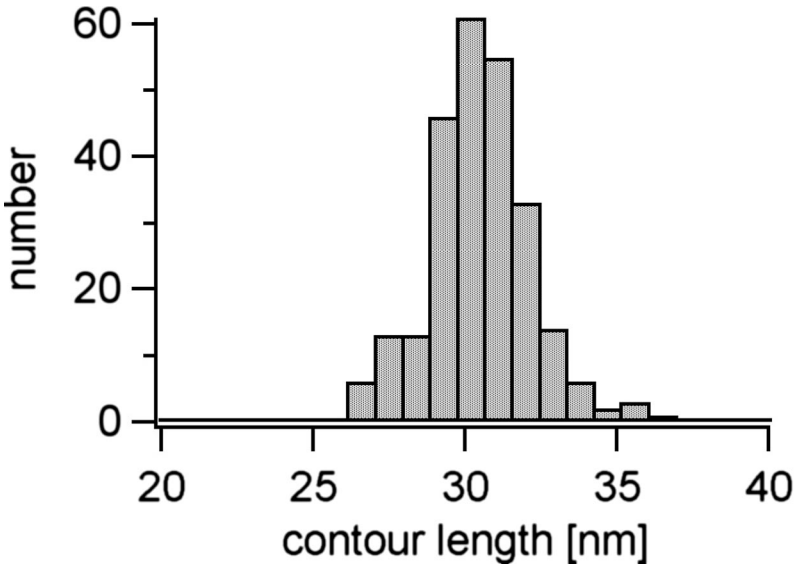

Fig. S4. Histogram of experimental Ig/Fn domain contour length increments. The values are obtained by transforming each trace with the QM-WLC model (persistence length $P = 0.8$ nm) into a barrier position histogram [Puchner EM, Franzen G, Gautel M, Gaub HE (2008) *Biophys J* 95:426–434] and by fitting the corresponding peaks with Gaussians. The mean value amounts to 30.45 nm, and the standard deviation values 1.68 nm.

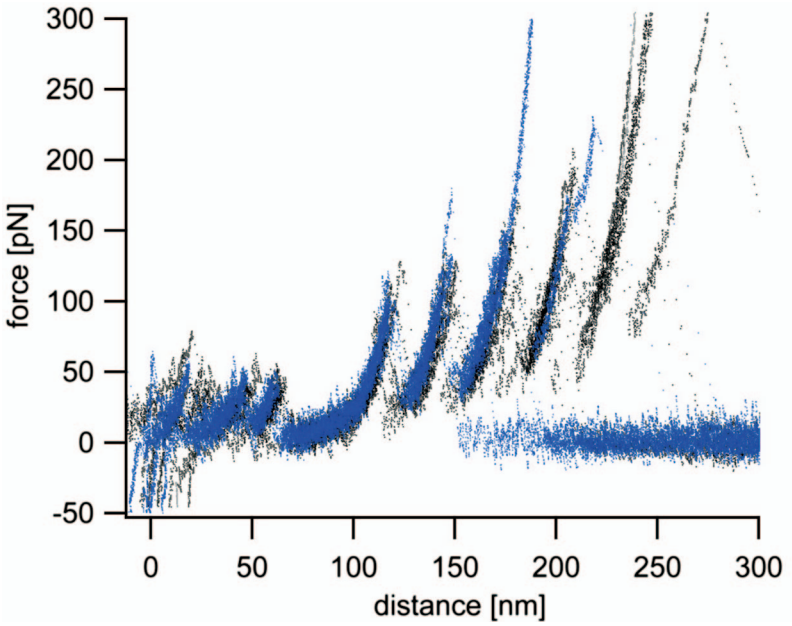

Fig. S5. Superposition of traces from different TK protein constructs. The traces in black show the unfolding of the *E. coli*-expressed protein construct consisting of five spacer domains whereas the other one contains only three spacer domains (blue). The maximum number of even spacings at the end of the traces ($\Delta L \approx$ 30 nm) reflects the number of spacer domains in both cases.

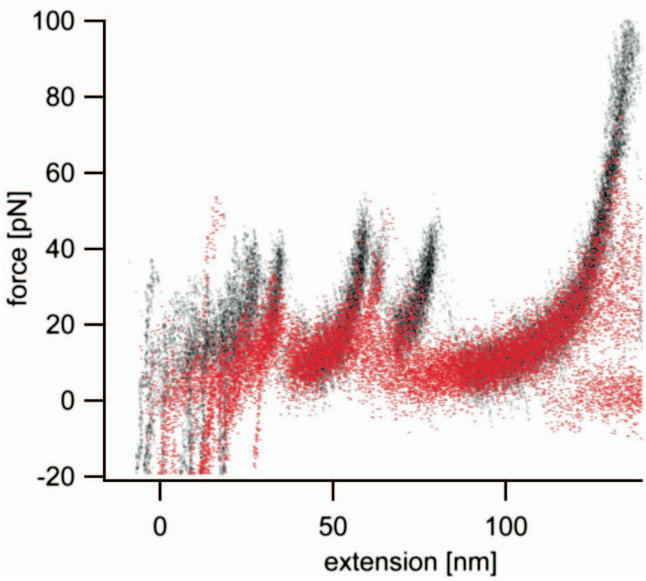

Fig. S6. Unfolding pattern of the titin kinase at 37°C. The black points show the superposition of traces recorded at room temperature, whereas the red traces were recorded at 37°C. Although the unfolding forces are smaller by ≈20 pN, the unfolding pattern is the same at 37°C.

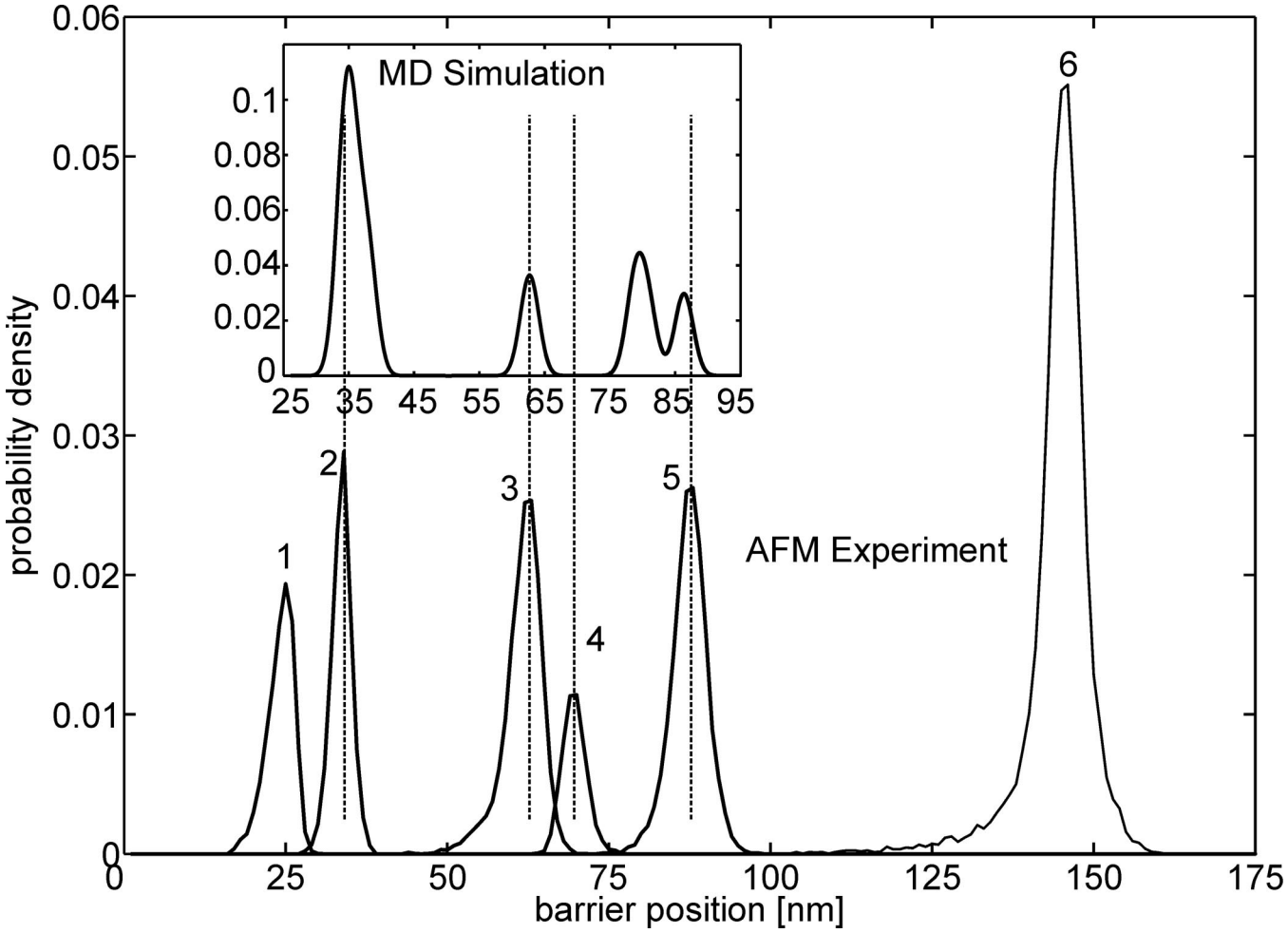

Fig. S7. Barrier positions from AFM experiments and MD simulations in the absence of ATP. The latter were obtained from the simulations of the complete TK (321 residues) shown in Fig. 3*B Bottom*. The positions of the force peaks obtained from the AFM experiments are indicated by the dashed lines.

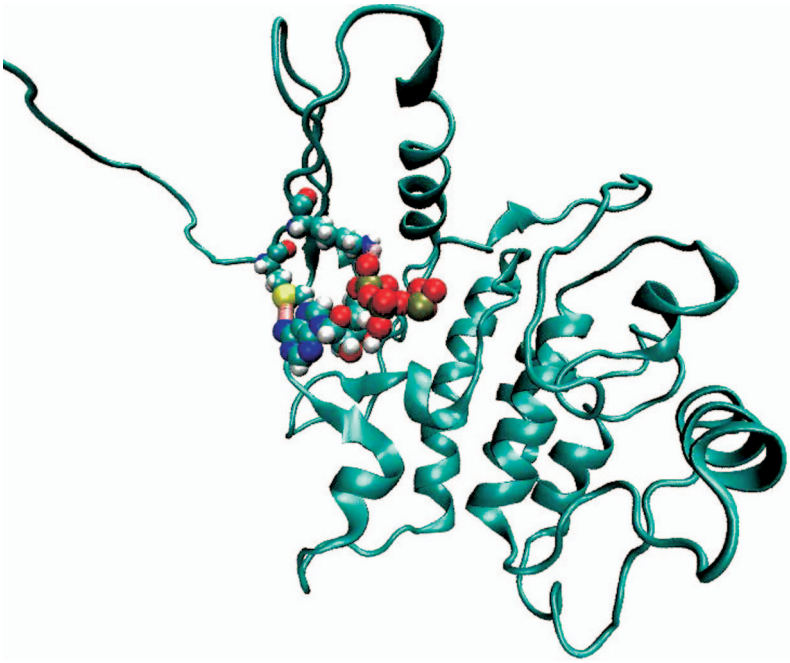

Movie S1. Structural changes during peak 2*: Unfolding of titin kinase (ribbon representation) upon mechanical stress, with ATP (ball-and-stick representation) bound to the active site. Interactions with ATP (dashed lines) cause an additional force peak (peak 2* in Fig. 2) in both the AFM experiment and the molecular dynamics simulations, which is not seen in the ATP-free state. Particularly strong interactions contributing to this peak are seen with Met-34 and Lys-36, which are shown in ball-and-stick representation. The bond with Met-34 with the purine base breaks before that of Lys-36 with the α-β phosphate groups.

Movie S1 (MPG)

Table S1. Conversion of residues in N2B titin (NP_003310.3) to the numbering in the titin kinase crystal structure 1TKI

Residue in 1TKI	Residue in N2B titin
Met-34	Met-24781
Lys-36	Lys-24783
Asp-127	Asp-24874
Tyr-170	Tyr-24917

Table S2. Expected experimental contour length increments of Ig/Fn-domain unfolding

Domain	Folded diameter, nm	No. of folded amino acids	Contour length increment, nm
A168 (PDB entry 2NZI)	4.3	95	30.74
A169 (PDB entry 2NZI)	4.8	101	32.07
A170 (PDB entry 2NZI)	4.0	95	30.68
M1 (PDB entry 2BK8)	4.1	93	29.95

The theoretical contour length increments were calculated by multiplying the number of folded amino acids with 0.365 nm and subtracting the diameter of the folded domains. The mean value amounts to 30.86 nm.

Table S3. Schematic structure of ATP (above), defining the atom numbers used in the tables, and atomic partial charges for ATP (below)

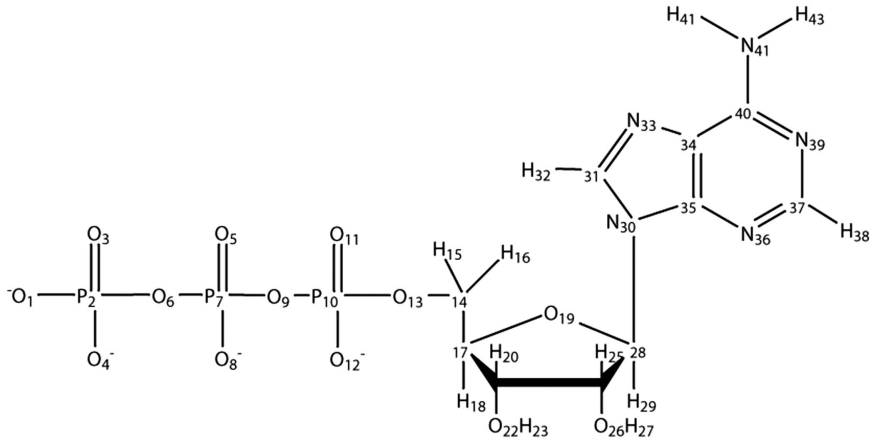

No.	OPLS type	Charge
1	lopls_969	−1.1
2	opls_966	1.9
3	opls_969	−1.1
4	opls_969	−1.1
5	opls_968	−0.6
6	opls_969	−1.1
7	opls_966	1.9
8	opls_969	−1.1
9	opls_968	−0.7
10	opls_966	1.9
11	opls_969	−1.1
12	opls_969	−1.1
13	opls_968	−0.7
14	opls_183	−0.12
15	opls_140	0.06
16	opls_140	0.06
17	opls_183	0.17
18	opls_140	0.03
19	opls_180	−0.6
20	opls_158	0.2
21	opls_140	0.06
22	opls_171	−0.68
23	opls_172	0.42
24	opls_158	0.2
25	opls_140	0.06
26	opls_171	−0.68
27	opls_172	0.42
28	opls_183	0.3
29	opls_140	0.06
30	opls_354B	−0.38
31	opls_353	0.2
32	opls_359	0.14
33	opls_352	0.2
34	opls_350	0.15
35	opls_349	0.38
36	opls_348	−0.55
37	opls_347	0.35
38	opls_355	0.2
39	opls_346	−0.53
40	opls_351	0.53
41	opls_356	−0.74
42	opls_357	0.385
43	opls_358	0.355

Table S4. Lennard–Jones (6, 12) parameters

OPLS type	*d*	*e*
opls_966	0.374	0.837
opls_967	0.350	0.276
opls_968	0.296	0.879
opls_969	0.296	0.879